International Journal of Nanomedicine

Dovepress
Taylor & Francis Group

Open Access Full Text Article

ORIGINAL RESEARCH

Macrophage Membrane Coated Manganese Dioxide Nanoparticles Loaded with Rapamycin Alleviate Intestinal Ischemia-Reperfusion Injury by Reducing Oxidative Stress and Enhancing Autophagy

Ruxiang Sheng[1,*], Wei Wang[2,*], Weian Zeng[3], Bin Li[4], Haoyuan Yu[5], Xuan Li[1], Yanqiu Liang[1], Ying Wang[1], Yuhui Liao[2], Dezhao Liu[1]

[1]Department of Anesthesiology, The Fifth Affiliated Hospital of Sun Yat-Sen University, Zhuhai, 519000, People's Republic of China; [2]Molecular Diagnosis and Treatment Center for Infectious Diseases Dermatology Hospital of Southern Medical University, Guangzhou, 510091, People's Republic of China; [3]Department of Anesthesiology, State Key Laboratory of Oncology in South China. Guangdong Provincial Clinical Research Center for Cancer, Sun Yat-Sen University Cancer Center, Guangzhou, 510060, People's Republic of China; [4]School of Inspection, Ningxia Medical University, Yinchuan, 750004, People's Republic of China; [5]Department of Hepatic Surgery and Liver Transplantation Center, The Third Affiliated Hospital of Sun Yat-Sen University, Guangzhou, 510630, People's Republic of China

*These authors contributed equally to this work

Correspondence: Yuhui Liao; Dezhao Liu, Email liaoyh8@mail.sysu.edu.cn; sumsldz@126.com

---

Background: Intestinal ischemia-reperfusion (I/R) injury is a common and severe clinical issue. With high morbidity and mortality, it burdens patients and the healthcare system. Despite the efforts in medical research, current treatment options are unsatisfactory, urging novel therapeutic strategies. Oxidative stress and dysregulated autophagy play pivotal roles in the pathogenesis of I/R injury, damaging intestinal tissues and disrupting normal functions. The aim of this study is to fabricate macrophage membrane-coated manganese dioxide nanospheres loaded with rapamycin [Ma@(MnO_2+RAPA)] for alleviating intestinal I/R injury.

Methods: We engineered honeycomb MnO_2 nanospheres coated with a macrophage membrane to act as a drug delivery system, encapsulating RAPA. In vitro OGD/R model in IEC-6 cells and in vivo mouse I/R injury models were used. Targeting ability was evaluated through in-vivo imaging system. Effects on cell viability, reactive oxygen species (ROS) levels, oxygen generation, inflammatory factors, apoptosis, autophagy, and biocompatibility were detected by methods such as MTT assay, fluorescence microscopy, ELISA kit, TUNEL assay, Western blotting and histological analysis.

Results: In this study, Ma@(MnO_2+RAPA) efficiently deliver RAPA to damaged tissues and exhibited good ROS-responsive release. Our data showed that Ma@(MnO_2+RAPA) reduced ROS, increased O_2, inhibited inflammation, and promoted autophagy while reducing apoptosis in IEC-6 cells. In a mouse I/R model, Ma@(MnO_2+RAPA) significantly reduced Chiu's score, improved tight conjunction proteins, decreased apoptosis, reduced levels of inflammatory cytokines and oxidative stress. RAPA released from the Ma@(MnO_2+RAPA), enhanced the expression of autophagy-regulated proteins p62, Beclin-1, and LC3II. The biocompatibility and safety of Ma@(MnO_2+RAPA) were confirmed through histological analysis and biochemical detection in mice.

Conclusion: Our results demonstrated that Ma@(MnO_2+RAPA) alleviated intestinal I/R injury by reducing oxidative stress, promoting autophagy, and inhibiting inflammation. This study offers a potential therapeutic strategy for the treatment of intestinal ischemia-reperfusion injury.

Keywords: ischemia reperfusion injury, biomimetic manganese dioxide nanoparticle, rapamycin, oxidative stress, reactive oxygen species

---

Received: 5 December 2024
Accepted: 12 March 2025
Published: 18 March 2025

Introduction

Ischemia/reperfusion is a common clinicopathological process that is strongly associated with various clinical conditions such as hemorrhagic shock, mesenteric ischemia, neonatal necrotizing enterocolitis, trauma, and organ transplantation.[1,2] Intestinal ischemia emerges when there exists a total or partial obstruction of blood flow to the intestines, leading to cell death and intestinal barrier dysfunction upon reperfusion. In these types of injury processes, systemic inflammatory response syndrome (SIRS) and multiple organ dysfunction syndrome (MODS) occur. Acute mesenteric ischemia (AMI) can have a mortality rate above 50%.[3–5] Currently, there is a lack of an effective treatment method for I/R in clinical practice. Thus, the exploration of effective drug therapies that specifically target intestinal damage caused by ischemia/reperfusion is essential.

Oxidative stress in conjunction with excessive activation of reactive oxygen species (ROS) exerts a vital part in the pathogenesis of intestinal I/R injuries.[6–10] The presence of ROS such as hydrogen peroxide (H_2O_2), hydroxyl (OH), superoxide anion (O^{2-}), nitric oxide radicals (NO) and others, along with the disruption of tight junctions and infiltration of commensal microbes into the tissue often leads to an elevated inflammatory response. This, in turn, causes damage to lipids, proteins, and DNA, ultimately resulting in apoptosis and necrosis of intestinal mucosal cells.[11] Undoubtedly, tissue and cell damage worsens when hypoxia occurs during the ischemia process. Given the evidence from previous studies demonstrating the role of reducing excessive ROS in cell death,[12] it is important to consider implementing effective reductive regimens. In this context, the limitations of using a single-agent for therapy has been often attributed to its nonspecific biodistribution after systemic administration, rapid clearance, and its relatively low capacity for scavenging ROS.[13] As a result, nanoparticles (NPs), which are nano-sized non-viral vectors, have been extensively utilized in drug delivery due to their controlled release capability and biodegradability.[14,15] In addition, the use of membrane coating nanotechnology endows NPs with targeting and immune evasion abilities.[16] Previous research has also demonstrated the use of macrophage membrane-coated NPs in the treatment of cerebrovascular and cardiovascular diseases.[17,18] In addition to their immune evasion ability, targeting capability, and biocompatibility, the free radical scavenging capability is an important factor to consider for certain reagents such as MnO_2, Prussian blue (PB), NiO, Pt, CeO_2, and others.[19,20] In particular, manganese oxides, which are affordable and easily accessible inorganic materials, have been widely utilized in various industries, including energy storage and medical biomaterials.[21–23] Manganese dioxide is a non-toxic material that has been frequently used for oxidation. When exposed to H^+ ions, it breaks down into Mn^{2+} ions, which are quickly eliminated by the kidneys.[24] Additionally, hydrogen peroxide (H_2O_2) comprises one of the prominent ROS, that plays a crucial role in maintaining redox homeostasis and various important biological processes in living organisms. However, excessive accumulation of hydrogen peroxide can be toxic to cells.[25] Manganese dioxide (MnO_2) nanoparticles facilitate the rapid breakdown of excess H_2O_2 into water and oxygen (O_2), resulting in the generation of an ani-ROS effect. Alternatively, the oxygen generated through the enzymatic digested of H_2O_2 by MnO_2 can alleviate the hypoxic environment.[26]

A considerable quantity of studies has demonstrated that autophagy has a crucial role in regulating intestinal I/R injury.[27–30] In this context, rapamycin (RAPA), also known as sirolimus, which was initially developed as a fungicide, has been currently used in several clinical applications for its immunosuppressive and antiproliferative effects, as well as its ability to inducive autophagy through mTOR.[31] Autophagy constitutes a cellular procedure whereby eukaryotic cells employ lysosomes to deteriorate their own cytoplasmic proteins and damaged organelles. This process is modulated by autophagy related genes (ATG) and is essential for maintaining cell growth, development, and homeostasis.[32–35] Autophagy enhances cell viability by eliminating damaged organelles and reducing oxidative stress.[36] Prior researchers have demonstrated that rapamycin has a shielding effect against hemangioma, vascular inflammation, osteoarthritis, and injuries to the kidney, heart, and brain caused by I/R.[37–39] However, the application of rapamycin is often restricted due to its adverse effects, including anemia and hyperlipidemia. Correspondingly, NPs have unique properties that enable them to overcome these limitations. The macrophage membrane coating on Ma@(MnO_2+RAPA) serves multiple purposes. Macrophages, being part of the immune system, can move freely in the body. Coating NPs with macrophage membranes allows Ma@(MnO_2+RAPA) to evade the immune detection.[40–43] The immune system recognizes the macrophage-like membrane as a "self" component, thus extending the circulation time of the nanoparticles in the bloodstream. Consequently, they have a higher chance of reaching the target site, the ischemic intestine, and reducing the exposure of the drug to non-target tissues, which minimizes drug toxicity and side effects.

In addition, the MnO_2 in Ma@(MnO_2+RAPA) has an inherent ability to decompose hydrogen peroxide (H_2O_2), a major ROS. The reaction $2H_2O_2 \rightarrow 2H_2O + O_2$ not only reduces the harmful levels of ROS in the ischemic intestinal environment but also generates oxygen. The generated oxygen can alleviate the hypoxic condition in the ischemic intestine, which is crucial for cell survival. Rapamycin (RAPA), encapsulated within the MnO_2 nanoparticles, is released when the nanoparticles reach the ischemic site. RAPA promotes autophagy by inhibiting the mTOR pathway. Autophagy helps cells clear damaged organelles and reduce oxidative stress, further enhancing the cell's ability to survive. The combination of ROS elimination, oxygen generation, and autophagy induction by Ma@(MnO_2+RAPA) works synergistically to treat ischemic intestines. These nanoparticles, Ma@(MnO_2+RAPA), which are capable of eliminating ROS and generating O_2 to salvage the ischemic intestine, were developed in the present study (Scheme 1). Therefore, the objective of this study is to fabricate Ma@(MnO_2+RAPA) nanoparticles for the treatment of intestinal I/R injury. By using this novel nanoparticle system, we aim to circumvent the toxic side-effects associated with the traditional administration of RAPA and to explore its potential in effectively treating intestinal I/R injury through mechanisms such as ROS elimination, O_2 generation, and autophagy promotion.

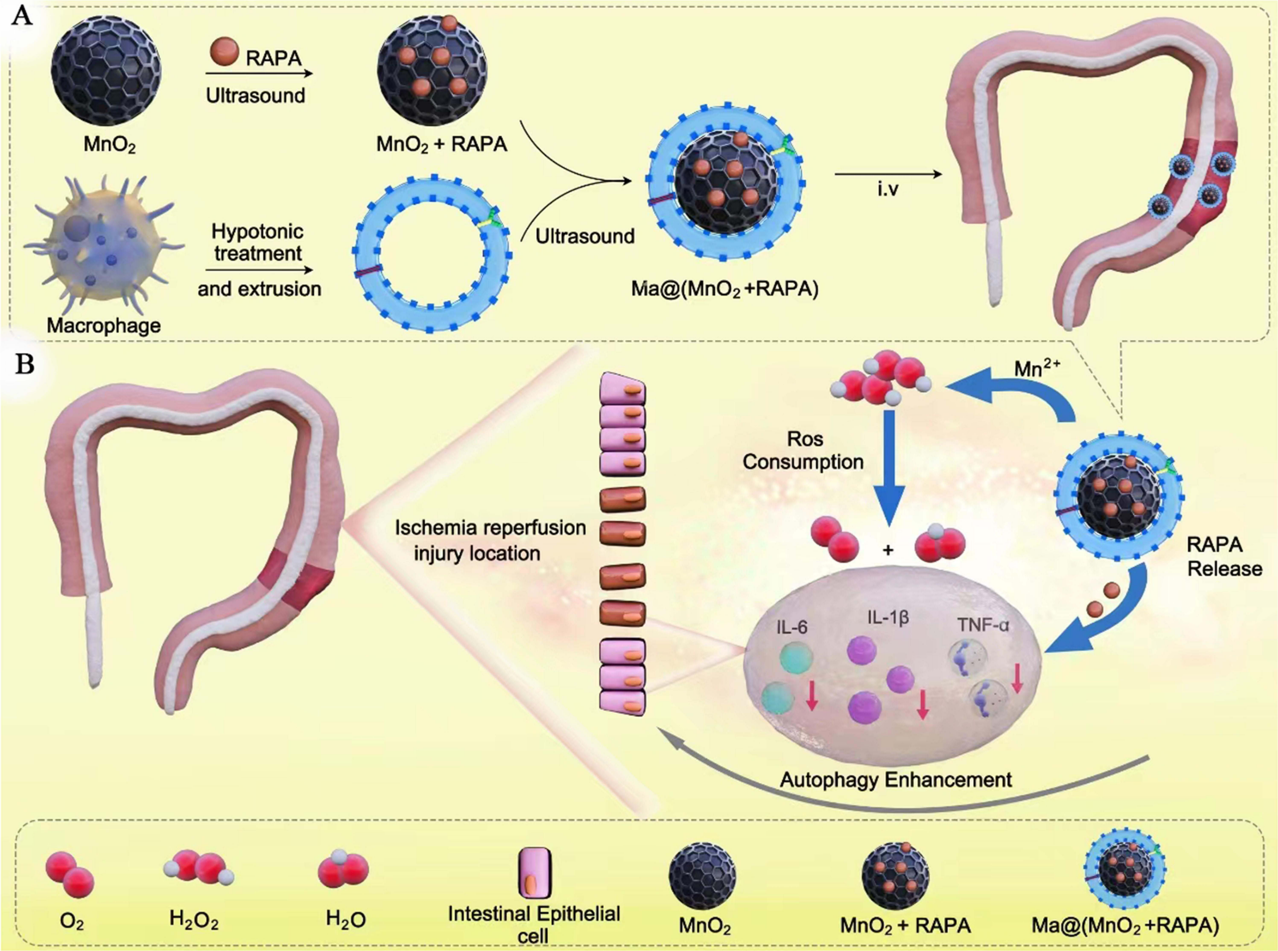

Scheme 1 Illustration of Ma@(MnO_2+RAPA) nanoparticles formation and alleviation of intestinal ischemia/reperfusion injury. (**A**) Scheme of the construction process of Ma@(MnO_2+RAPA) nanoparticles. (**B**) Demonstration of Ma@(MnO_2+RAPA) nanoparticles therapy for intestinal ischemia/reperfusion injury. Coating with macrophage membranes endows Ma@(MnO_2+RAPA) nanoparticles with aggregation capacity forward to damaged intestinal tissues. Ma@(MnO_2+RAPA) nanoparticles could rescue damaged cells by consuming excessive ROS, producing O_2, prohibiting pro-inflammation, and activating autophagy.

Materials and Methods

Materials

Methanol and ethanol were acquired from Machlin Biochemistry (Shanghai, China). Oleic acid (OA) (≥99%) was purchased from Duly Biotech Co., Ltd. (Nanjing, China). Potassium permanganate ($KMnO_4$) was acquired from Baijun Tech (Guangzhou, China). RAPA was acquired from Coolaber Science & Technology Co., Ltd (Beijing, China). The methyl thiazolyl tetrazolium (MTT) compound was procured from Labgic Technology Co., Ltd. (Beijing, China). The ELISA kits for mouse malondialdehyde (MDA), superoxide dismutase (SOD), TNA-α, IL-6, and IL-1β, were obtained from Bolaz Biotechnology Co., Ltd. (Nanjing, China). The autophagy assay kit was procured from AAA Bioquest (California, USA).

The following antibodies were obtained from Cell Signaling Technology (Massachusetts, USA): a rabbit monoclonal antibody to Beclin-1 (D40C5), a rabbit polyclonal antibody to SQSTM1/p62, a rabbit polyclonal antibody to LC3B, a rabbit antibody to β-actin, and a goat monoclonal antibody to rabbit IgG. The ROS detection kit was obtained from Servicebio Biology Co., Ltd (Wuhan, China).

Vascular clips were procured from Kerong Biotechnology Co., Ltd. (Guangzhou, China).

Cell lines: Rat intestinal epithelial cells, specifically IEC-6 cells, were purchased from Bolaz Biotech Co., Ltd. (Nanjing, China). IEC-6 cells were cultured in DMEM medium containing 100 mg mL^{-1} streptomycin, 10% foetal bovine serum (FBS), and 100 U mL^{-1} penicillin. The cells were raised at a temperature of 37 °C in a controlled environment with added moisture and 5% CO_2.

Animals

Male C57BL/6 mice with an age of 8 weeks, were obtained from Ruige Biotech Co., Ltd. (Guangzhou, China). The interventions and animal care procedures were implemented in conformity with the Animal Surgery Guidelines and Policies for provided by the Animal-related Ethics Panel of the Fifth Affiliated Hospital, Sun Yat-sen University (No. 00520) (Zhuhai, China). The mice were accommodated in a controlled setting where the temperature range of 24–25 °C, and the humidity was at 55%. They were placed under a 12-hour light/12-hour dark cycle pattern, and hand unrestricted access to food and water. The mouse intestinal ischemia/reperfusion model was established as follows: The mice were anesthetized by injecting 3% pentobarbital sodium into their peritoneal cavity. The superior mesenteric artery (SMA) was meticulously exposed and securely ligated at its distal end using a clamp. Subsequent to the occlusion of blood flow to the SMA for 1 h, the vascular clip was taken off to allow reperfusion for an additional twenty-four hours. In the control group, the vascular clip was removed promptly upon reaching the SMA.[44] The mouse intestinal IR model closely mimics the clinical situation, enabling a comprehensive evaluation of nanoparticle efficacy, targeting, and systemic effects. Nevertheless, it is associated with individual variations and complex operations. In addition to clamping the SMA, the intestinal I/R model can also be prepared by clamping the abdominal aorta. However, this method can simultaneously cause I/R injury to other abdominal organs, and is more often used to study related issues such as multiple organ dysfunction.[45] Mice were randomly separated into six groups, each consisting of three mice. The groups were dealt with in the following ways: sham (saline, iv)., I/R (saline, iv)., I/R+RAPA (1.5 mg kg^{-1}), I/R+Ma@MnO_2 (with an equivalent dosage of 3 mg kg^{-1} MnO_2), I/R+MnO_2+RAPA (with an equivalent dosage of 3 mg kg^{-1} MnO_2), I/R + Ma@(MnO_2+RAPA) (with an equivalent dosage of 3 mg kg^{-1} MnO_2).

The alveolar macrophage membrane was derived from MH-S cells, a murine alveolar macrophage cell line procured from the American Type Culture Collection (ATCC). The cells were cultivated in suspension flasks using RPMI 1640 medium (Gibco) augmented with 1% penicillin-streptomycin (Gibco) and also 10% foetal bovine serum (Hyclone). The cells were cultured in T-175 flasks until they reach a high concentration and were then collected by centrifugation at a speed of 700 × g for 5 minutes. The cells were cleansed with PBS (500 × g for 10 minutes), and thereafter the cell pellet was made to be suspended in the homogenization buffer which contained 10 mm KCl (Sigma), 75 mm sucrose, 20 mm Tris·HCl (pH = 7.5, MediaTech), 2 mm $MgCl_2$ (Sigma), and a single tablet of protease/phosphatase inhibitor (Pierce, Thermo Fisher Scientific). The suspension mixture was then added to a Dounce homogenizer, which was disrupted with 15 to 35 strokes. Subsequently, the suspension was subject to centrifugation at 800 × g for 5 minutes in order to eliminate large remnants. Subsequently, the supernatant portion was gathered and centrifugated at 10000 × g for 25 minutes, and then the pellet was spread out, while the supernatant portion was again centrifuged at 150000 × g for 50 minutes. Then, the supernatant portion was suspended and the membrane was obtained in the form of an off–white pellet. A solution of 1×10^{-3} M ethylenediaminetetraacetic acid (EDTA; Sigma) in H_2O was then used to wash the membrane pellet. Subsequently, the pellet was subjected to gentle sonication for further testing.[46] Then quantification of membrane protein quantity was conducted using the Pierce BCA assay (Life Technology).

Preparation of MnO_2, Ma@MnO_2, MnO_2+RAPA, and Ma@(MnO_2+RAPA) Nanospheres

A solution of $KMnO_4$ (200 mg) was fully dispersed in 100 mL of deionized water, afterward OA (2233.5 mg) was incorporated subsequent to 1 hour of agitation. The mixture was kept at ambient temperature for a period of 24 hours until the black product formed. The products were collected through centrifugation with a velocity of 12000 rpm for a time span of 20 minutes. The material was then rinsed twice with alcohol and distilled water to remove any remaining substances.[47] The purified MnO_2 was dispersed in distilled water and analyzed using an inductively-coupled plasma-mass spectrometric analysis (ICP-MS) for preparing honeycomb MnO_2 solution possessing a concentration of 0.5 mg mL^{-1}. The samples' crystallographic configuration and elemental constitution were evaluated using X-ray diffraction (XRD) and energy dispersive spectrometry (EDS), respectively, in sequence. The unique surface morphology and distribution of pore sizes in comb-like MnO_2 were identified using conventional N_2 adsorption-desorption analysis. A quantity of RAPA powder (10 mg) was introduced into a solution of honeycomb MnO_2 in water (10 mL) and ultrasonicated for 1 h to result in MnO_2+RAPA. The surplus RAPA was eliminated via centrifugation. During the process, RAPA was effectively attached to the layer of comb-like MnO_2 through electrostatic adhesion. The amount of drug present was determined using the ultraviolet-visible spectroscopy (UV-vis). In order to create Ma@(MnO_2+RAPA) NPs, MnO_2+RAPA were blended with vesicles of macrophage membrane and made to pass across 200 nm polycarbonate porous membranes on 30 occasions. The Ma@ MnO_2 NPs were prepared in the same way. The size and charge of synthesized NPs were determined using dynamic light scattering (DLS), while the shapes of the NPs were examined using transmissive electron microscopy (TEM) and scanning electron microscopy (SEM). The simple synthesis of MnO_2 nanoparticles leads to good stability, as its single-component structure is less likely to be affected by external factors. Compared with the soft-chemical method used in this study for synthesizing honeycomb-like MnO_2 nanoparticles, the electrochemical method requires sophisticated production equipment and incurs relatively high production costs. However, it enables precise control over the formation rate of MnO_2 and its crystal structure.[48]

Ultraviolet–Visible Spectroscopy (UV-Vis) Method

The loading efficiency was determined using UV-vis spectroscopy with a UV detector set to a wavelength of 279 nm.

The Release of RAPA From Ma@(MnO_2+RAPA) in vitro

Ma@(MnO_2+RAPA) NP solutions (1 mg mL^{-1}, 5 mL) were introduced into a disposable dialysis bag (Slide-A-Lyzer MINI Dialysis Units, MWCO:3500 Da, Thermo Scientific). The bag was subsequently placed in a petri dish containing 10 mL of PBS, either with or without 100×10^{-6} M H_2O_2. At 2 hours, 4 hours, 6 hours, 8 hours, 10 hours, and 12 hours, 2 μL of an external drug release buffer were collected. The absorbance at 279 nm was gauged using UV-vis spectroscopy in order to ascertain the concentration of the drug.

ROS Scavenging of MnO_2

The ability of MnO_2, Ma@ MnO_2, MnO_2+RAPA, and Ma@(MnO_2+RAPA) NPs to eliminate ROS was assessed by measuring the remaining H_2O_2 levels after incubating with the NPs for specific time periods. 1.0 mL of MnO_2 with various concentration (0.01, 0.02, 0.1, and 0.5 mg mL^{-1}) was combined with 9.0 mL of an H_2O_2 solution (10×10^{-6} M). After incubation for 0, 1, 2, 3, and 4 h, the amount of H_2O_2 remaining was measured using the H_2O_2 assay kit. The identical procedure was carried out on MnO_2+RAPA and Ma@(MnO_2+RAPA) NPs.

O_2 Catalytic Generation by MnO_2

The capacity of MnO_2 NPs to generate O_2 through catalysis was measured using a portable device that detects dissolved O_2. A solution of H_2O_2 (100×10^{-6} M) was mixed with two separate concentrations of MnO_2 (0.01 and 0.1 mg mL^{-1}). The mixture was allowed to react for 10 minutes, and the concentration of dissolved O_2 was measured every 2 minutes.

Cell Viability

Cell viability was determined using MTT, which stands for 3-(4,5)-dimethylthiazol(-z-y1)-3, 5-di-phenytetrazoliumromide. 96-well plates were incubated with 5×10^4 IEC-6 cells/well subsequently cultivated for twenty-four hours.[49] The original medium was substituted with DMEM-adequate medium that contained varying concentrations of RAPA, Ma@MnO_2, MnO_2+RAPA, and Ma@(MnO_2+RAPA) nanoparticles for twenty-four hours. Subsequently, the cells were rinsed using PBS thereafter incubated with 50 µL of medium supplemented with 0.5 mg mL^{-1} MTT per well for four hours. Thereafter, the cells were rinsed using PBS once more, and 150 µm DMSO was introduced into each well with the aim of dissolving the formazan that had formed. Ten minutes later, absorbance at 540 nm was recorded.

IEC-6 Cell Oxygen Glucose Deprivation/Reoxygenation (OGD/R) Model

IEC-6 cells were plated in 96-well plates where the density was 5×10^4 cells for each well and were cultivated for twenty-four hours. The cells were washed using PBS; thereafter, the medium was substituted by PBS. The cells were then cultivated in a hypoxia incubator (Binder) for 12 h. Subsequently, the medium was switched to DMEM universal medium for two hours.[50]

ROS Eliminating Ability of Ma@(MnO_2+RAPA) in OGD/R Model

The intracellular levels of ROS were ascertained using H2DCFDA, also known as 2',7'-dichlorodihydrofluorescein diacetate. IEC-6 cells were plated in a 6-well plate where the density was 8×10^5 cells each well. Thereafter, the cells were treated with a solution of PBS that contained RAPA, MnO_2, and Ma@(MnO_2+RAPA) under OGD for a time span of 12 hours. Subsequently, the cells were exposed to a complete medium containing H2DCFDA (10 µM) for 30 minutes following a prior wash with PBS. The fluorescence microscope was used to measure the intensity of green fluorescence.

O_2 Productive Ability of Ma@(MnO_2+RAPA) in OGD/R Model

The intracellular concentration of ROS was measured using [(Ru(dpp)3)]Cl_2 (RDPP), a fluorescence probe that is highly sensitive to molecular oxygen and can undergo a significant reduction in fluorescence intensity. IEC-6 cells were grown in a 6-well plate where the density was 8×10^5 cells each well. Subsequently, the cells were cultivated in a solution of PBS containing RAPA, Ma@MnO_2, MnO_2+RAPA, and Ma@(MnO_2+RAPA) under conditions of OGD for 12 h. Subsequently, the cells were exposed to a comprehensive medium supplemented with RDPP (10 µL, 10 mg L^{-1}) for a duration of 4 hours, following a prior wash with PBS. The fluorescence microscope was used to measure the intensity of red fluorescence.

Internalization of Ma@(MnO_2+RAPA) in IEC-6 Cells

IEC-6 cells were grown in a 6-well plate where the density was 8×10^5 cells each well and incubated for twenty-four hours. Thereafter, the cells were rinsed with PBS and then exposed to a medium containing DiD-labelled Ma@(MnO_2 +RAPA) for 4 h. Fluorescence intensity was then captured via Confocal Laser Scanning Microscope (CLSM) analysis.

Western Blotting

Immunoblotting analysis was utilized to determine the secretion levles of Beclin-1, p62, and LC3B. The samples were collected from the intestinal mucosa and IEC-6 cells. The researcher gathered intestinal tissues and blended them in a solution containing 4% paraformaldehyde. IEC-6 cells were placed in a 6-well plate where the density was 8×10^5 cells every well. They were then cultured in PBS under OGD conditions for 12 h. After that, they were incubated with a complete medium containing RAPA (0.94 µg mL^{-1}), Ma@MnO_2, MnO_2+RAPA, and Ma@(MnO_2+RAPA) NPs (equal dose of 1.88 µg mL^{-1}) for two hours. The samples were subjected to treatment with RIPA lysis buffer before applying the

BCA method to determine the protein concentration. A total of 15 micrograms of the entire protein sample were segregated using a 12.5% (w/v) SDS-PAGE gel for electrophoresis and subsequent to transferring onto polyvinylidene fluoride films. The membranes were initially blocked with a 5% (w/v) solution of fat-free dry milk. They were then exposed to anti-β-actin (1:1000), beclin-1 antibody (1:1000), p62 antibody (1:1000), and LC3B antibody (1:1000). Thereafter, the membranes were placed in incubation with a secondary antibody attached to peroxidase (1:2000). The protein marker was determined using chemiluminescence compounds and analyzed using the Invitrogen iBright system (Thermo Fisher, USA).

Histological Analysis of Intestinal Injury

The intestinal sections were stabilized using hematoxylin and eosin (H&E). Damage to the intestinal mucosa was then estimated using the Chiu's scoring system.[51] The intestinal mucosa injury was determined by assessing and averaging the results of six selected fields of each mouse.

In Situ TUNEL Assay of Intestinal Mucosa Apoptosis

The intestinal sections were fixed in a 4% paraformaldehyde solution and embedded in paraffin. The presence of apoptotic cells was confirmed using terminal deoxynucleotidyltransferase (TdT)-driven dUDP-biotin nick end labeling (TUNEL). The apoptotic level was evaluated by calculating the apoptotic index, which amounts to the ratio of TUNEL-positive cells to the total number of cells.

Measurement of Cytokines

Specimens were derived from serum, isolated intestinal tissues, or cell culture supernatant. The left colon, which was separated from the other tissues, was broken down and dissolved using RIPA cleavage buffer. The concentrations of TNF-α, IL-6, IL-1β, MDA, and SOD in the samples were quantified using the ELISA kit, following the specified protocol.

Targeting Ability of Ma@(MnO_2+RAPA) on Intestinal I/R Model

After 2 hours of reperfusion, intestinal I/R mice received an injection of free DiOC18(3) or Ma@(MnO_2+RAPA) labeled with DiOC18(3) along the tail vein. The In Vivo Imaging System (IVIS) was utilized to capture images of the mice at 12-hour and 24-hour intervals following reperfusion. The colons, hearts, spleens, livers, kidneys, and lungs on the left side were isolated and imaged using IVIS at 24 h after reperfusion.

Statistical Analysis

The data underwent analysis using Statistical Product and Service Solutions 26 (SPSS). The results were manifested in the form of the average value along with plus or minus the standard deviation (SD). The statistical significance among groups was evaluated by means of one-way ANOVA and non-parametric tests. The significance levels were signified as $^{*}P < 0.05$, $^{**}P < 0.01$, and $^{***}P < 0.001$.

Results and Discussion

Preparation and Characterization of Ma@(MnO_2+RAPA)

The synthesis of honeycomb MnO_2 nanoparticles was achieved using a ameliorated soft chemistry mode.[52] Simply put, at room temperature within distilled water, potassium permanganate ($KMnO_4$) was reduced through oleic acid (OA). During this process, OA functioned as both a synthetic template and a reducing agent, while MnO_2 nuclei formed on the surface of OA-formed emulsified oil wastewater created by OA. The process of loading rapamycin was achieved through ultrasonication for a duration of 1 hour. Finally, Ma@MnO_2 and Ma@(MnO_2+RAPA) were prepared using an extrusion method. The UV-vis absorption spectra revealed the emergence of a new wide peak at approximately 233 nm, while the primary peaks of $KMnO_4$ (320, 526, and 545 nm) disappeared upon completion of the reaction, indicating the formation of honeycomb MnO_2 (Figure S1). The elemental composition of the samples was subject to analysis using energy-

https://doi.org/10.2147/IJN.S507546

dispersive spectroscopy (EDS). The EDS pattern (Figure S2), clearly indicated that the atomic ratio of Mn to O was close to 1:2, thus confirming the presence of MnO_2. Additionally, the use of transmission electron microscopy (TEM) and scanning electron microscopy (SEM) (Figure 1A-C; Figure S3) revealed the honeycomb spherical structure of MnO_2 and Ma@(MnO_2+RAPA). The XRD analysis revealed that the presence of dominant peaks was at 2θ=10.59°, 12.08°, 36.96°, and 65.87°, corresponding to the lattice planes (001), (002), (100), and (110) of MnO_2, respectively (Figure S4). Moreover, the self-assembled nanospheres were found to have a size of ~110 nm (Figure 1A). Furthermore, the mean hydrodynamic diameter of MnO_2, Ma@MnO_2, MnO_2+RAPA, and Ma@(MnO_2+RAPA) was approximately 100.6 nm, 121.0 nm, 104.2 nm, and 120.2 nm, respectively. Additionally, the ζ potentials of MnO_2, Ma@MnO_2, MnO_2+RAPA, and Ma@(MnO_2+RAPA) were determined to be −40.3 mV, −21.9 mV, −40.8 mV, and −22.7 mV, respectively (Figure 1D), using dynamic light scattering (DLS). As observed, the average hydrodynamic diameter of Ma@MnO_2 and Ma@(MnO_2 +RAPA) were slightly greater than those of MnO_2 and MnO_2+RAPA because of the inclusion of macrophage membranes. In addition to the above, the specific surface area and pore size distribution of MnO_2 nanospheres were investigated using the N_2 adsorption-desorption method. The honeycomb MnO_2 had a BET surface area of ~4.35 $m^2g,^{-1}$ with the majority of the pores having a size of 4.6 nm (Figures S5 and S6, Supporting Information). Additionally, to assess the stability of Ma@(MnO_2+RAPA) under physiological conditions, the NPs were placed in

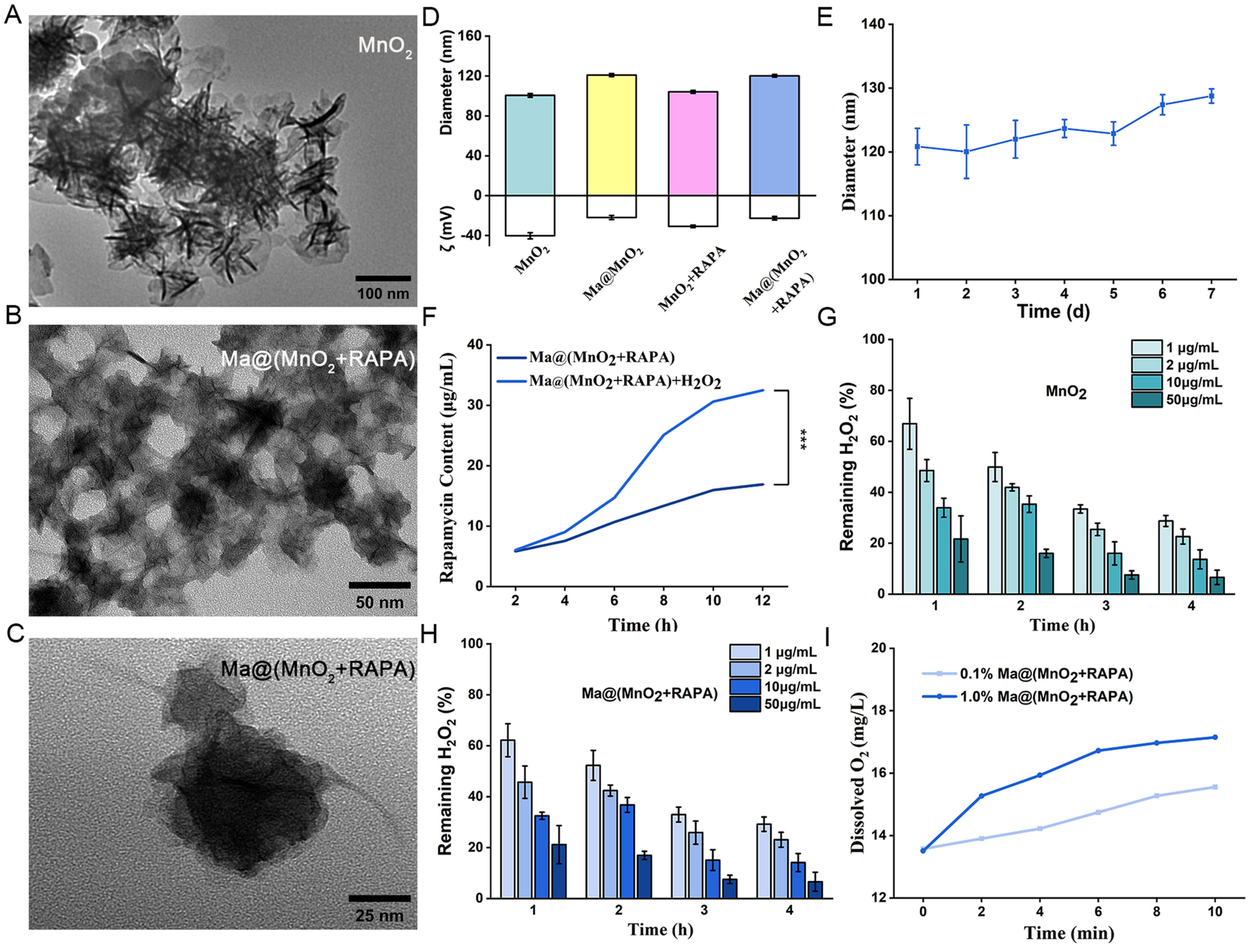

Figure 1 Characterizations of macrophage membrane-coated MnO_2 nanoparticles. (**A**) Representative TEM images of the honeycomb MnO_2 nanoparticles (inner scale bar, 100 nm). (**B** and **C**) Representative TEM images of Ma@(MnO_2+RAPA) nanospheres (inner scale bar, 50 nm and 20 nm, respectively). (**D**) Zeta-potential and size distribution of MnO_2, Ma@MnO_2, MnO_2+RAPA, and Ma@(MnO_2+RAPA). (**E**) The size distribution of Ma@(MnO_2+RAPA) in 10% FBS over 1 week. Results are presented as mean ± SD, n=3. (**F**) The in vitro release of RAPA from Ma@(MnO_2+RAPA) with and without 100×10^{-6} M H_2O_2 in PBS. Results are presented as mean ± SD, n=3. (**G**) Scavenging H_2O_2 ability of MnO_2 with different concentrations over 4 hours. Results are presented as mean ± SD, n=3. (**H**) Scavenging H_2O_2 ability of MnO_2 with different concentrations over 4 hours. Results are presented as mean ± SD, n=3. (**I**) The changes of O_2 concentration in 100×10^{-6} M H_2O_2 after different concentration of MnO_2 were added. Results are presented as mean ± SD, n=3.

a solution of 0.01 M PBS (pH 7.4) under conditions of room temperature for 7 days. No discernible changes in size could be observed, which was ascribed to the existence of hydrophilic surface glycan proteins in the phospholipid cell membrane molecule (Figure 1E).

Herein, rapamycin was loaded onto the NPs by subjecting it to ultrasonication with a suspension of manganese dioxide for 1h. Subsequently, the residual drug was eliminated through the process of centrifugation. During intestinal I/R, a significant quantity ROS was generated and accumulated, resulting in the rapid release of RAPA from the activated nanomedicine. As observed from the results, the concentration of RAPA steadily increased over time and reached the maximum limit for drug release at 10 h. Subsequently, the drug-loading capacity of MnO_2 was investigated using UV-vis spectroscopy. In the absence of H_2O_2, the loading efficiency was ~20% at 12 h in 0.01 M phosphate-buffered saline (PBS), thus mimicking the pathophysiological status. However, the presence of H_2O_2, the loading efficiency increased to 50% at the same time point (Figure 1F). Subsequently, the as-obtained nanomedicine was covered using alveola macrophage membrane in order to improve its stability and targeting capabilities.

ROS Scavenging and O_2-Producing Properties of Ma@(MnO_2+RAPA)

Excessive production and accumulation of ROS during intestinal ischemia/reperfusion can cause cell apoptosis, epithelial barrier dysfunction, and cell death. This can lead to an uncontrolled inflammatory response, thereby resulting in systemic inflammatory response syndrome (SIRS) and multiple organ dysfunction syndrome (MODS).[53] Particularly, abnormal levels of H_2O_2 have been strongly linked to ischemia/reperfusion injury cancer, and various other diseases.[54] Thus, the consumption of excessive H_2O_2 in order to promote the regeneration of damaged intestinal cells appears essential. During reperfusion, hypoxia occurs and worsens, to increase cell deaths. To address this, MnO_2 NPs were utilized in the current study to alleviate hypoxia in an acidic environment. The ability of MnO_2 in neutralizing ROS was assessed by quantifying the residual concentration of H_2O_2 after incubation with varying concentrations of MnO_2 for specific durations. The results indicated that the concentration of residual H_2O_2 decreased gradually as the concentrations of MnO_2, Ma@MnO_2, MnO_2+RAPA, and Ma@(MnO_2+RAPA) increased (Figure 1G and H; Figure S7). These results strongly support our finding that Ma@(MnO_2+RAPA) can effectively reduce oxidative stress and improve the hypoxic environment in ischemic intestines, which is crucial for protecting intestinal cells during IR injury. This suggests that the elimination process is dependent on the concentration of the NPs. Correspondingly, the generation of O_2 was observed using a portable dissolved oxygen detector. The decrease in residual H_2O_2 concentration was observed to be time dependent. In all groups that included MnO_2, more than 60% of H_2O_2 was used within 1 h. However, there was no discernible difference between membrane coated MnO_2, and RAPA-loaded MnO_2 coated with membrane NPs. In addition, the rate of oxygen production reached its peak within the first two minutes. Thus, the capability of MnO_2 NPs to remove H_2O_2 was not affected by the presence of RAPA or the coating of the membrane. The findings demonstrated a direct correlation between the generation of O_2 and the consumption of H_2O_2 (Figure 1I). Thus, the high encapsulation efficiency and effective scavenging capability of the synthetic nanomedicine towards H_2O_2 were confirmed.

The Protective Effects of Ma@(MnO_2+RAPA) in Vitro

The increase in ROS during intestinal I/R is one of the most important mechanisms of intestinal cell death. Building upon the efficient scavenging ability of H_2O_2 exhibited by the synergic NPs, the underlying mechanisms responsible for the protective effects of Ma@(MnO_2+RAPA) NPs on the intestines were explored using an ex vivo approach. Accordingly, an oxygen-glucose deprivation/reoxygenation (OGD/R) model was utilized to imitate ischemia/reperfusion injury in IEC-6 cells.[55] For the purpose of evaluating the targeted delivery of Ma@(MnO_2+RAPA) to intestinal cells treated with OGD, IEC-6 cells were exposed to either Ma@(MnO_2+RAPA) (Control) or DiD-labelled Ma@(MnO_2+RAPA) [DiD+Ma@(MnO_2+RAPA)] (Figure 2A). The results indicate that IEC-6 cells incubated with DiD+Ma@(MnO_2+RAPA) exhibited a stronger red fluorescence compared to the cells incubated with Ma@(MnO_2+RAPA) (Figure 2B). Notably, the use of RAPA at a concentration of 0.94 $\mu g\ mL^{-1}$, Ma@MnO_2 and Ma@(MnO_2+RAPA) at a concentration of 1.88 $\mu g\ mL^{-1}$ (with an equal dose of 1.88 $\mu g\ mL^{-1}$ MnO_2) resulted in the optimum viability of IEC-6 cells (Figure 2C; Figure S8). However, cytotoxicity was likely induced when the concentration of RAPA exceeded 7.5 $\mu g\ mL^{-1}$, possibly

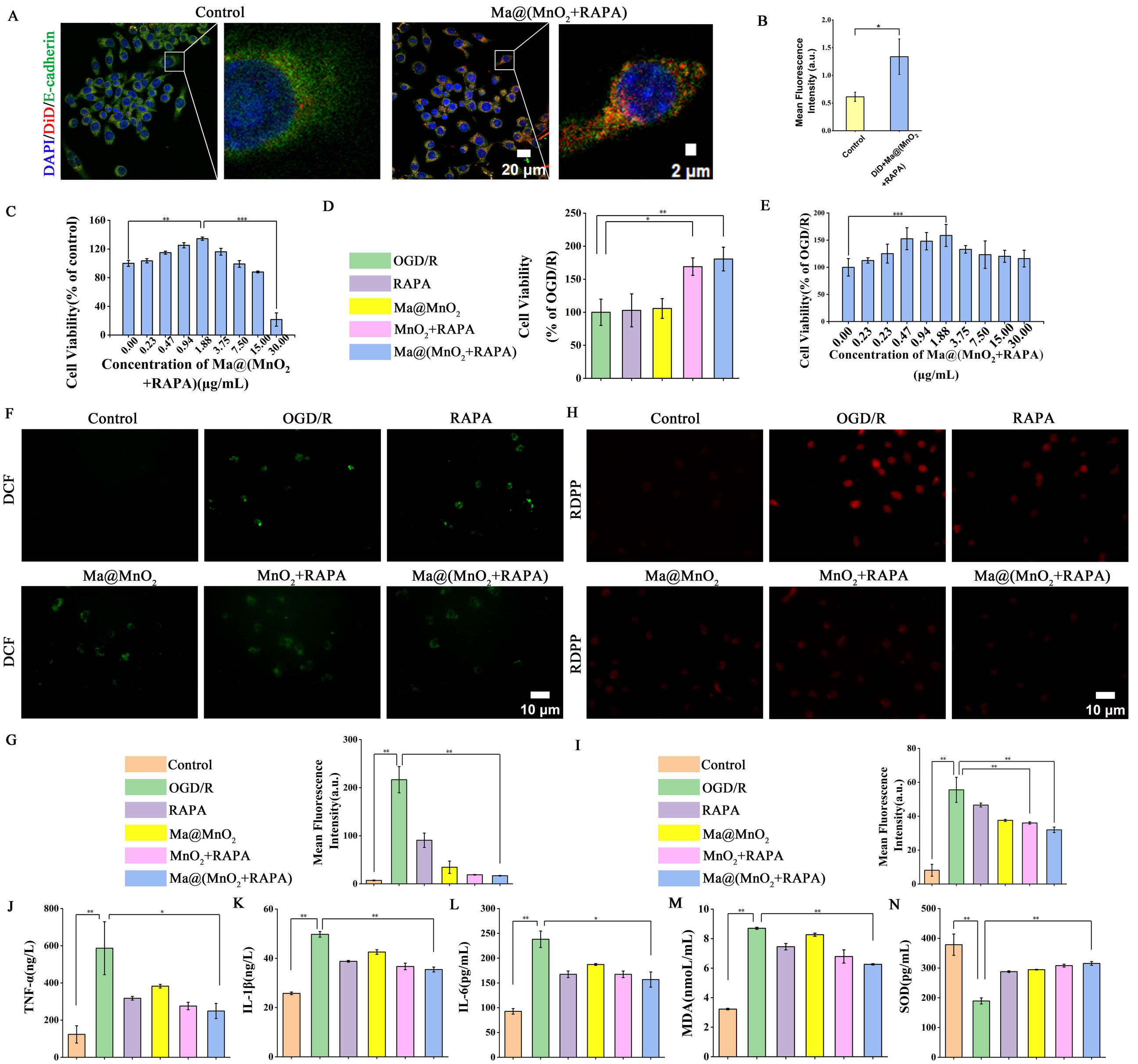

Figure 2 Protective effects of Ma@(MnO$_2$+RAPA) in vitro. (**A**) Representative LSCM images of increased DiD-labeled Ma@(MnO$_2$+RAPA) accumulation in IEC-6 cells. (**B**) Quantitative analysis of red fluorescence of DiD-labeled Ma@(MnO$_2$+RAPA) NPs. Results are presented as mean ± SD, n=3. $^{*}P < 0.05$, $^{**}P < 0.01$. (**C**) The cell viability of IEC-6 cells after incubation with different concentrations of Ma@(MnO$_2$+RAPA) for 24 hours. Results are presented as mean ± SD, n=3. $^{**}P < 0.01$. (**D**) The cell viability of IEC-6 cells after being incubated with Ma@(MnO$_2$+RAPA) at 1.88 μg mL^{-1} with the treatment of OGD at 12 hours. Results are presented as mean ± SD, n=3. $^{***}P < 0.001$. (**E**) The cell viability of IEC-6 cells after being incubated with different concentrations of Ma@(MnO$_2$+RAPA) following treatment OGD at 12 hours. Results are presented as mean ± SD, n=3. $^{***}P < 0.001$. (**F**) Representative images of ROS detected by H2DCFDA in IEC-6 cells (scale bar,10 μm). (**G**) Quantitative analysis of green fluorescence of ROS. Results are presented as mean ± SD, n=3. $^{*}P < 0.05$, $^{**}P < 0.01$. (**H**) Representative images of O$_2$ generated in IEC-6 cells (scale bar, 10 μm). (**I**) Quantitative analysis of red fluorescence of O$_2$. Results are presented as mean ± SD, n=3. $^{*}P < 0.05$, $^{**}P < 0.01$. (**J-N**) Inflammatory factors (TNF-α, IL-1β and IL-6) and oxidative stress factors (SOD and MDA) contained in cell culture supernatant. Results are presented as mean ± SD, n=3. $^{*}P < 0.05$, $^{**}P < 0.01$.

as a result of excessive autophagy. Furthermore, the impact of various NPs on the survival of IEC-6 cells at varying oxygen-glucose (OGD) durations was examined. The findings revealed that the extent of cell damage was most pronounced after 12 h of OGD, whereas the combination of Ma@(MnO$_2$+RAPA) was most effective in mitigating this damage (Figure 2D; Figure S9). Accordingly, IEC-6 cells treated with OGD/R + Ma@(MnO$_2$+RAPA) at a concentration of 1.88 μgmL,–^{1} with an equal dose of MnO$_2$, showed a significant improvement in cell viability in comparison to those treated with OGD/R alone (Figure 2E). Additionally, the combination of Ma@(MnO$_2$+RAPA) effectively decreased the amount of ROS within IEC-6 cells following OGD/R, as measured using detected by 2’,7’-

dichlorodihydrofluorescein diacetate (H2DCFDA) (Figure 2F). Among different groups, the green fluorescent intensity of cells treated with OGD/R+Ma@(MnO_2+RAPA) underwent a significant reduction (Figure 2G). Subsequently, an oxygen sensing probe (RDPP) was used to measure the generation of O_2 in relation to IEC-6 cells. The fluorescence intensity of the RDPP probe is weakened by the dynamic quenching of molecular oxygen. As observed from the findings (Figure 2H), the level of O_2 significantly increased within the IEC-6 cells that were treated with OGD/R+Ma@(MnO_2 +RAPA) in comparison to those treated with OGD/R, OGD/R+RAPA, OGD/R+Ma@MnO_2, and OGD/R+ MnO_2 +RAPA. However, the administration of RAPA failed to promote the generation of O_2, while its addition did not induce any discernible effects on the ability of Ma@(MnO_2+RAPA) NPs to produce O_2 (Figure 2I). Conversely, the oxygen generated by MnO_2 NPs mitigated cell deaths due to microcirculatory dysfunction.[56] Simultaneously, MnO_2 NPs were able to alleviate oxidative conditions, thereby significantly improving cell viability.[57] The presence of significant amount of inflammatory cytokines, along with oxidative stress during intestinal I/R, is a significant contributing factor to intestinal cell damage.[58] Consequently, inhibiting the proinflammatory microenvironment in order to reduce the severity of ischemia/reperfusion injury is deemed essential. As a result, the levels of TNF-α, IL-1 β, and IL-6 were measured. A significant decrease in these cytokines was observed in IEC-6 cells treated with OGD/R+Ma@(MnO_2+RAPA) in comparison to other nanomedicine groups (Figure 2J–L). In addition, the Ma@(MnO_2+RAPA) nanomedicine effectively reduced oxidative stress, as evidenced by the alterations in MDA and SOD levels in the cell culture supernatant (Figure 2M and N). Thus, the results demonstrated that the synergic nanomedicine exhibited effective cell targeting, as well as antioxidative and anti-inflammatory effects.

In addition to the above, the consequences of the flow cytometry analysis demonstrated that Ma@(MnO_2+RAPA) significantly reduced the apoptosis rate in IEC-6 cells (Figure 3A and B). Thus, Ma@(MnO_2+RAPA) was found to effectively prevents apoptosis in IEC-6 cells by eliminating ROS and generating O_2. Meanwhile, a remarkable increase in autophagy was observed in IEC-6 cells treated with OGD/R+Ma@(MnO_2+RAPA) (Figure 3C and D). The Western blotting results (Figure 3E–H) demonstrated that the expression of proteins p62, beclin-1, and LC3II increased in IEC-6 cells treated with OGD/R+Ma@(MnO_2+RAPA). This suggests that the protective effects of Ma@(MnO_2+RAPA) against oxidative stress may be attributed to its ability to activate autophagy.

Targeting Capability of Ma@(MnO_2+RAPA) to the Ischemic Intestine in Vivo

Previous studies have demonstrated the remarkable ability of macrophage membrane-coated nanoparticles to aggregate specifically and evade the immune system. Herein, the targeting efficacy of the Ma@(MnO_2+RAPA) NPs was evaluated in a mouse model of intestinal I/R using an IVIS-system. Noticeable clustering of Ma@(MnO_2+RAPA) NPs occurred in the affected region 12 and 24 h after injection of DiO-labelled membrane-encapsulated nanoparticles through the tail vein in intestinal I/R mice (Figure 4A–C). Conversely, the brightness of the Ma@(MnO_2+RAPA) NPs was particularly noticeable in the intestinal tissues (Figure 4A–D). Interestingly, Ma@(MnO_2+RAPA) NPs were also accumulated in the lungs (Figure 4A–D), suggesting that the lungs may have been affected during the intestinal I/R injury.

Ma@(MnO_2+RAPA) Alleviated the Intestinal I/R Injury

Subsequently, the defensive effects of Ma@(MnO_2+RAPA) NPs against intestinal ischemia/reperfusion injury were investigated using a mouse model of intestinal I/R. After a 60-minute period of reduced blood flow (ischemia), the mice were divided into five groups. This was followed by a 120-minute period of restored blood flow (reperfusion). Two hours later, a solution of saline (0.5 mL, I/R group), pure RAPA (1.5 mg kg^{-1}, 0.5mL, RAPA group), Ma@MnO_2 (with the same dose of 3 mg kg^{-1} MnO_2, 0.5 mL, Ma@MnO_2 group), MnO_2+RAPA (with an equal dose of 3 mg kg^{-1} MnO_2, 0.5 mL, MnO_2+RAPA group), and Ma@(MnO_2+RAPA) (with the same dose of 3 mg kg^{-1} MnO_2, 0.5 mL, Ma@(MnO_2 +RAPA) group) were administered via the tail vein. The intestinal tissues were collected 24 hours after reperfusion for subsequent analysis. As observed from the results (Figure 5A), the control group exhibited a normal mucosal morphology, while the I/R group displayed significant oedema and loss of intestinal villi. According to Chiu's scoring system, the Ma@(MnO_2+RAPA) group had less intestinal mucosal injury compared to the I/R group (Figure 5B). Additionally, the immunohistochemical staining of OCCLUDIN and ZO-1 proteins in the mouse intestine showed that the integrity of the intestinal mucosal barrier was better preserved in the Ma@(MnO_2+RAPA) group in comparison to the I/R group

https://doi.org/10.2147/IJN.S507546

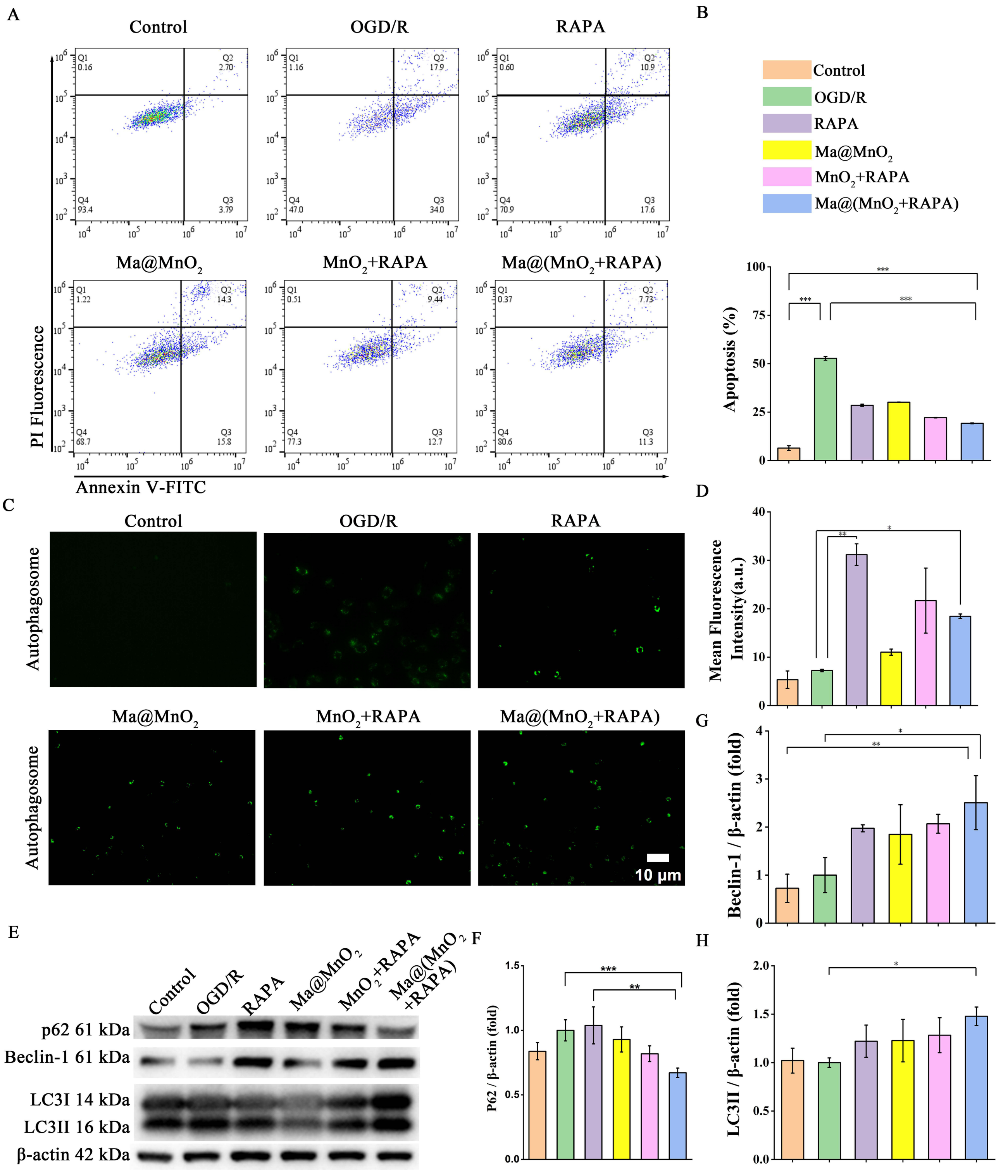

Figure 3 The effects of Ma@(MnO_2+RAPA) on apoptosis and autophagy in IEC-6 cells. (**A**) Flow cytometry results of apoptosis of IEC-6 cells. (**B**) Flow cytometry analysis of apoptosis of IEC-6 cells. Results are presented as mean ± SD, n=3. *$P < 0.05$, **$P < 0.01$. (**C**) Representative images of autophagosomes produced in IEC-6 cells (scale bar, 10μm). (**D**) Quantitative analysis of green fluorescence of autophagosomes. Results are presented as mean ± SD, n=3. *$P < 0.05$, **$P < 0.01$. (**E**) Expression of autophagy related proteins (P62, Beclin-1, and LC3II) characterized by Western blotting. (**F-H**) Detection of the relative protein expression intensities of P62, Beclin-1, and LC3II by Western blotting. Results are presented as mean ± SD, n=3. *$P < 0.05$, **$P < 0.01$, ***$P < 0.001$.

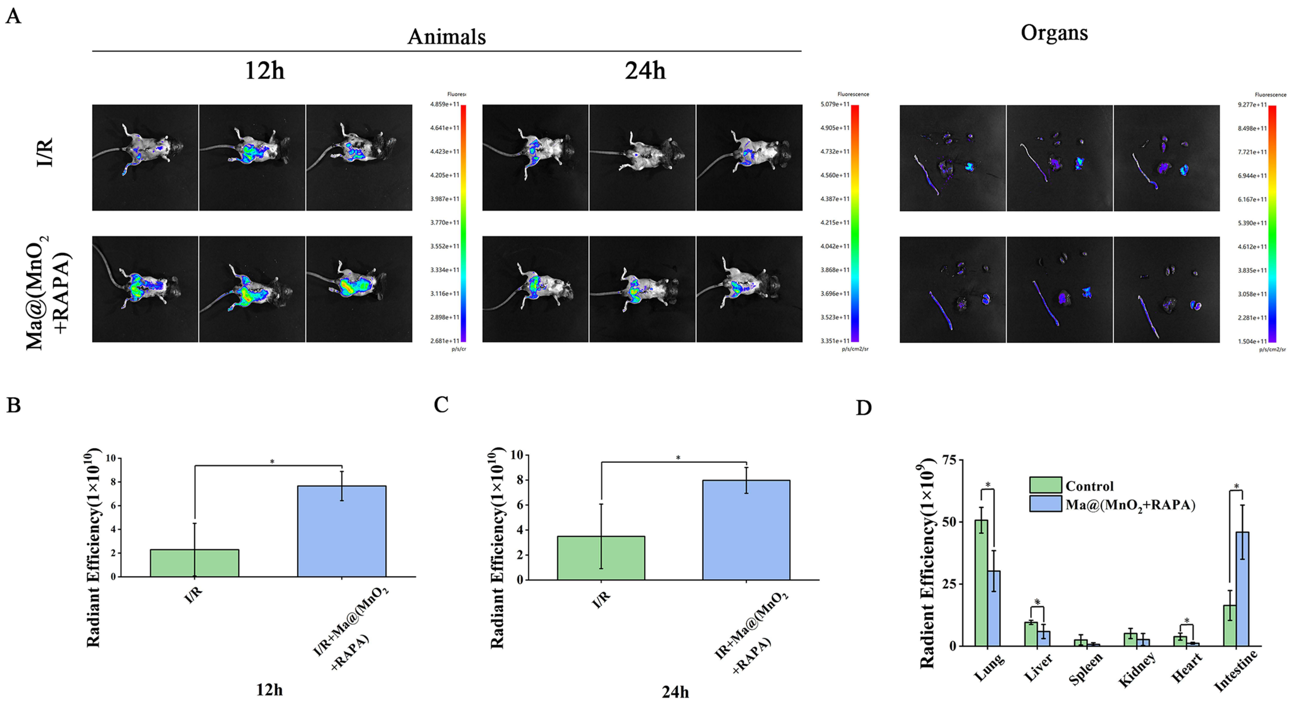

Figure 4 Targeting capability of Ma@(MnO_2+RAPA) to the ischemic intestine in vivo. (**A**) In vivo IVIS imaging of DiO-labeled Ma@(MnO_2+RAPA) in mice at 12 h and 24 h and major organs at 24 h. Radiant efficiency of fluorescence intensity of DiO-labeled Ma@(MnO_2+RAPA) in mice after (**B**)12 h and (**C**) 24h post-injection. Results are presented as mean ± SD, n=3. $^*P < 0.05$. (**D**) Radiant efficiency of fluorescence intensity of DiO-labeled Ma@(MnO_2+RAPA) in organs after 24 h post-injection. Results are presented as mean ± SD, n=3. $^*P < 0.05$.

(Figure 5A–D). Furthermore, terminal deoxynucleotidyl transferase dUTP nick-end labeling (TUNEL) staining disclosed that there was a significant greater proportion of apoptotic cells in the Ma@(MnO_2+RAPA) group in opposition to the I/R group (Figure 5A–E). The magnitudes of cytokines, specifically TNF-α, IL-1β, and IL-6, were prominently decreased subsequent to the administration of Ma@(MnO_2+RAPA) NPs (Figure 5F–H). As a result, Ma@(MnO_2+RAPA) NPs were able to reverse the proinflammatory microenvironment and restore the integrity of injured intestinal cells. Furthermore, the Ma@(MnO_2+RAPA) nanomedicine was detected to have a significant effect on reducing oxidative stress in mice. This was evidenced through the decline in serum MDA concentration and the increase in SOD levels in the Ma@(MnO_2+RAPA) group (Figure 5I and J). In addition, the results of Western blotting assay (Figure 5K–N) indicated that the expression of p62, beclin-1, and LC3II proteins was improved in the Ma@(MnO_2+RAPA) group. This suggests that the regulation of autophagy in this group aligns with the findings from the cell-based experiments. In other words, Ma@(MnO_2+RAPA) NPs provided protection against intestinal I/R injury by promoting autophagy. Thus, the modulation of autophagy may offer novel treatment options for ischemia/reperfusion injury.

The Biocompatibility of Ma@(MnO_2+RAPA) Nanoparticles

Finally, the biocompatibility of Ma@(MnO_2+RAPA) nanoparticles was assessed in vivo. Healthy mice were injected with Ma@(MnO_2+RAPA) NPs via their tail veins. Herein, a saline solution was used as the experimental control. The H&E staining of lung, liver, spleen, kidney, and heart tissue sections subsequent to treatment with Ma@(MnO_2+RAPA) NPs revealed no noticeable abnormal or inflammatory cell infiltration (Figure 6A). Consistently, serum biochemical assays measuring aspartate aminotransferase (AST), alanine aminotransferase (ALT), blood urea nitrogen (BUN), and creatinine (CREA) showed no noticeable abnormalities one week after daily NP administration (Figure 6B–D). Since the CREA levels of both groups were below the detection limit of 17.3 μmol L^{-1}, no statistical analysis was performed. Meanwhile, the changes in mice's body weight after injection were recorded over a period of 7 days. The resultant findings confirmed the favorable safety profile of the developed nanomedicine. The development of Ma@(MnO_2+RAPA) nanoparticles and the demonstration of their protective effects on intestinal cells align perfectly with our study's objective

https://doi.org/10.2147/IJN.S507546

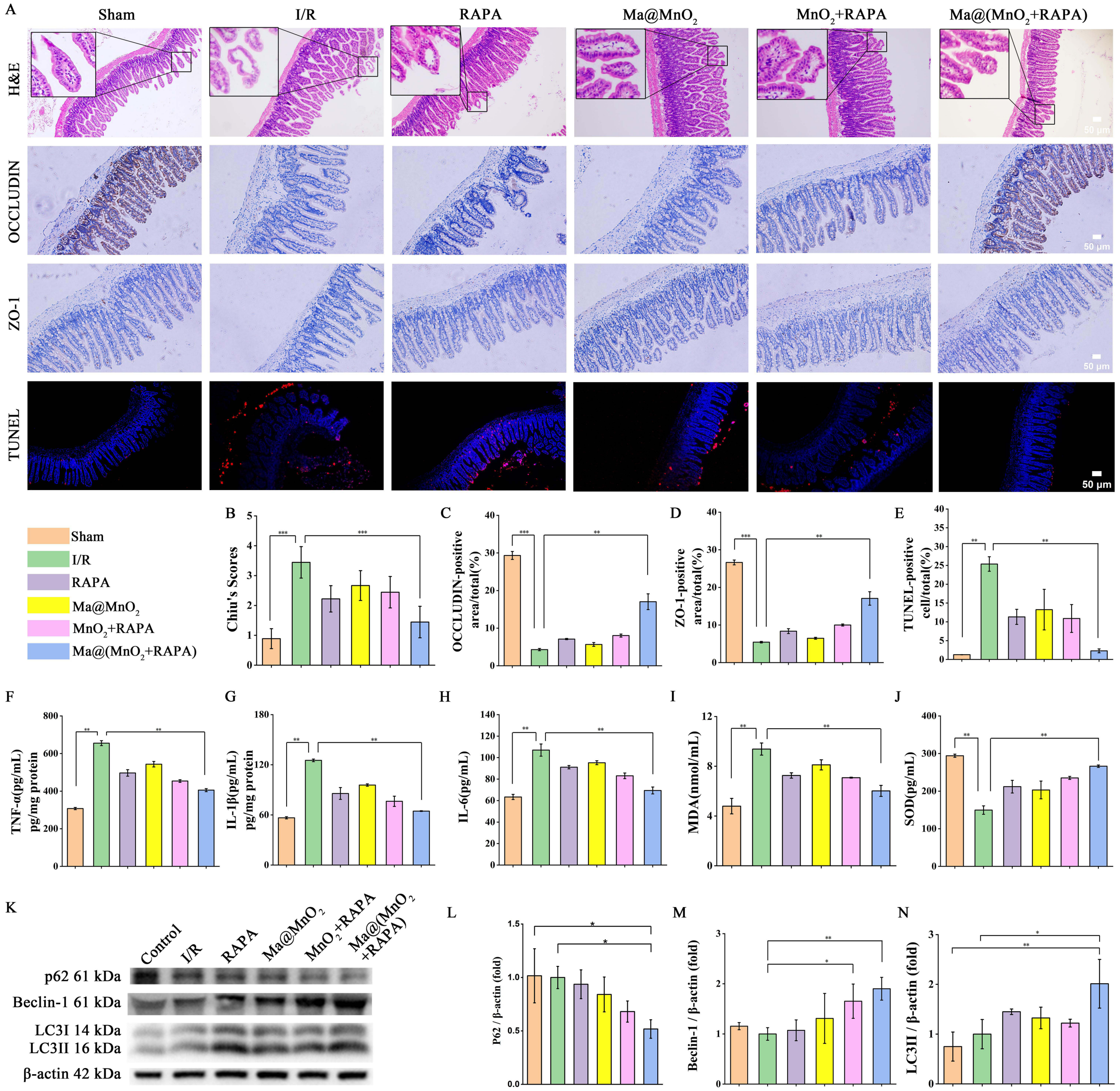

Figure 5 Ma@(MnO$_2$+RAPA) alleviated the intestinal I/R injury. (**A**) Representative images of H&E, OCCLUDIN, ZO-1, and TUNEL staining. (**B**) Quantification analysis of Chiu's scores, (**C**) OCCLUDIN, (**D**) ZO-1, and (**E**) TUNEL staining of treated mice. In the H&E staining images, the region outlined by the local magnification box exhibits distinct histological alterations typical of intestinal mucosal damage. These alterations include vacuolar degeneration and disorganization of the mucosal architecture. Results are presented as mean ± SD, n=3. $^{*}P < 0.05$, $^{**}P < 0.01$, $^{***}P < 0.001$. (**F-J**) Relative cytokine expression of TNF-α and IL-1β of treated mice. Results are presented as mean ± SD, n=3. $^{*}P < 0.05$, $^{**}P < 0.01$. (**H-J**) Serum levels of IL-6, SOD and MDA. Results are presented as mean ± SD, n=3. $^{*}P < 0.05$, $^{**}P < 0.01$. (**K**) Representative images of P62, Beclin-1, and LC3 characterized by Western blotting. (**L-N**) Detection of the relative protein expression intensities of P62, Beclin-1, and LC3II by Western blotting. Results are presented as mean ± SD, n=3. $^{*}P < 0.05$, $^{**}P < 0.01$.

of creating a novel treatment for intestinal I/R injury. In the broader context of nanomedicine, our findings offer a new perspective on the design and application of nanoparticle-based therapies for this challenging clinical condition. The unique combination of functions in Ma@(MnO$_2$+RAPA) not only addresses the multiple pathological factors in intestinal I/R injury but also provides a potential model for developing targeted nanotherapeutics. Despite the promising results of this study, it is important to note that the long-term effects of continuous exposure to Ma@(MnO$_2$+RAPA) nanoparticles remain unclear. Although our current in vitro and in vivo experiments have shown good biocompatibility in the short -

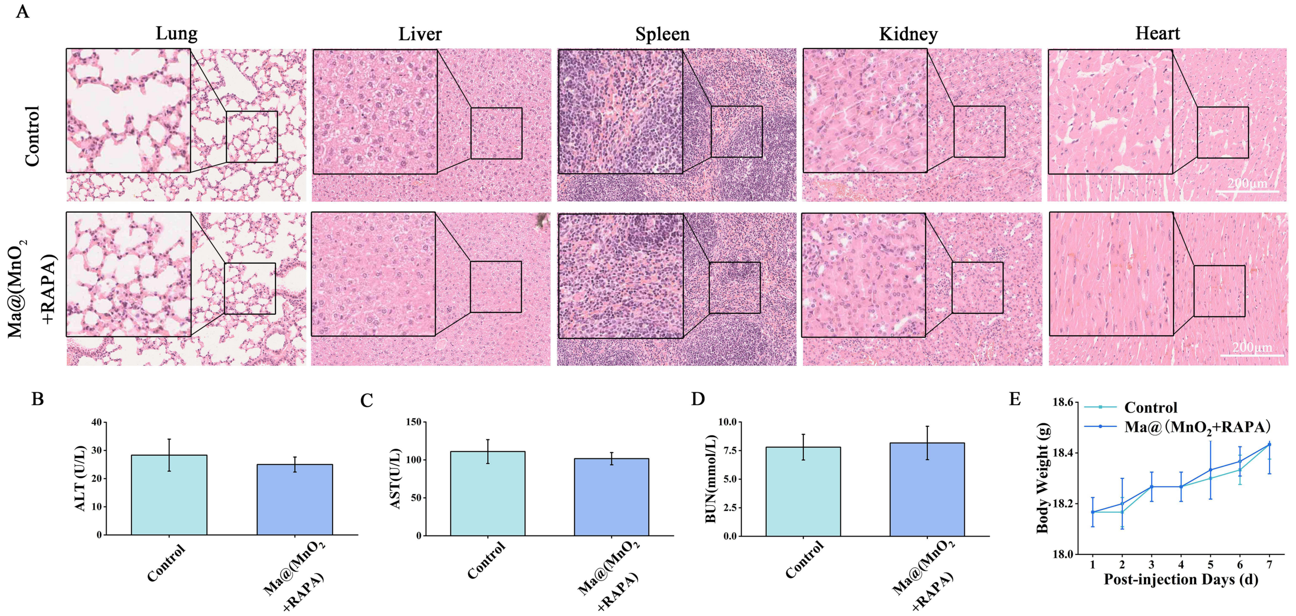

Figure 6 Assessing the biocompatibility of Ma@(MnO$_2$+RAPA). (**A**) Histochemistry analysis of lung, liver, spleen, kidney, and heart sections stained with hematoxylin-eosin. In the H&E staining images, the region outlined by the box represents the area selected for local magnification. (**B**–**D**) Biochemical parameters are indicative of hepatic and kidney functions: AST, ALT, and BUN. Results are presented as mean ± SD, n=3. (**E**) Mice body weight changes post-injection over 7 days. Results are presented as mean ± SD, n=3.

term, cumulative effects over an extended period may lead to unforeseen toxicity. This could potentially limit the long - term clinical application of Ma@(MnO$_2$+RAPA), and thus, further long-term studies are warranted.

Conclusion

In summary, we have achieved the successful synthesis of Ma@(MnO$_2$+RAPA) nanoparticles. Notably, these approximately 120 nm honeycomb-structured nanoparticles exhibit an enhanced capacity for RAPA release in the presence of H_2O_2. In vitro experiments demonstrated that Ma@(MnO$_2$+RAPA) nanoparticles effectively enhanced the viability of IEC - 6 cells. They significantly reduced the levels of ROS, increased O_2 production, inhibited the inflammatory response, promoted autophagy, and simultaneously decreased apoptosis. In vivo, Ma@(MnO$_2$+RAPA) nanoparticles were observed to specifically target the ischemic intestines in mice. They reduced the oxidative stress-mediated inflammatory response, enhanced autophagy, alleviated intestinal injury, and meanwhile, exhibited good biocompatibility. Therefore, our findings suggest that Ma@(MnO$_2$+RAPA) nanoparticles, by modulating oxidative stress, hypoxia, inflammation, and autophagy, hold potential as a novel treatment for intestinal I/R injury, offering a promising clinical approach and new treatment possibilities for related diseases.

Acknowledgments

This study was financially sustained by National Science Foundation of China (NO.82070542).

Disclosure

The authors declare no competing interest in this work.

References

1. OhC J, Kim M-J, Lee J-M, et al. Inhibition of pyruvate dehydrogenase kinase 4 ameliorates kidney ischemia-reperfusion injury by reducing succinate accumulation during ischemia and preserving mitochondrial function during reperfusion. *Kidney International*. 2023;104(4):724–739. doi:10.1016/j.kint.2023.06.022.
2. Zhang M, Liu Q, Meng H, et al. Ischemia-reperfusion injury: molecular mechanisms and therapeutic targets. *Signal Trans Target Therap*. 2024;9 (1):12. doi:10.1038/s41392-023-01688-x.

3. Bala M, Catena F, Kashuk J, et al. Acute mesenteric ischemia: updated guidelines of the world society of emergency surgery. *World J Emerg Surg*. 2022;17(1):54. doi:10.1186/s13017-022-00443-x.
4. Yu H, Kirkpatrick IDC. Kirkpatrick I D C an update on acute mesenteric ischemia. *Canad Associat Radiolog Jl*. 2022;74(1):160–171. doi:10.1177/08465371221094280.
5. Chen Y, Han B, Guan X, et al. Enteric fungi protect against intestinal ischemia–reperfusion injury via inhibiting the SAA1-GSDMD pathway. *J Adv Res*. 2024;61:223–237. doi:10.1016/j.jare.2023.09.008
6. Chu C, Wang X, Yang C, et al. Neutrophil extracellular traps drive intestinal microvascular endothelial ferroptosis by impairing fundc1-dependent mitophagy. *Redox Biol*. 2023;67:102906. doi:10.1016/j.redox.2023.102906
7. Cui Z, K AF, Zhao X, et al. Potential therapeutic effects of milk-derived exosomes on intestinal diseases. *J Nanobiotechnol*. 2023;21(1):496. doi:10.1186/s12951-023-02176-8
8. Hou M, Chen F, He Y, et al. Dexmedetomidine against intestinal ischemia/reperfusion injury: a systematic review and meta-analysis of preclinical studies. *Eur J Pharmacol*. 2023;959:176090. doi:10.1016/j.ejphar.2023.176090.
9. Wang X, Shen T, Lian J, et al. Resveratrol reduces ROS-induced ferroptosis by activating SIRT3 and compensating the GSH/GPX4 pathway. *Mol Med*. 2023;29(1):137. doi:10.1186/s10020-023-00730-6.
10. Hou M, Li X, Chen F, et al. Naringenin alleviates intestinal ischemia/reperfusion injury by inhibiting ferroptosis via targeting YAP/STAT3 signaling axis. *Phytomedicine*. 2024;135:156095. doi:10.1016/j.phymed.2024.156095.
11. Toghiani R, S A, Najafi H, et al. Bioengineering exosomes for treatment of organ ischemia-reperfusion injury. *Life Sci*. 2022;302:120654. doi:10.1016/j.lfs.2022.120654
12. Yang S-C, Wang Y-H, Ho C-M, et al. Targeting formyl peptide receptor 1 with anteiso-C13-surfactin for neutrophil-dominant acute respiratory distress syndrome. *Br J Pharmacol*. 2023;180(16):2120–2139. doi:10.1111/bph.16073
13. Liu J, Wang Y, Heelan WJ, et al. Mucoadhesive probiotic backpacks with ROS nanoscavengers enhance the bacteriotherapy for inflammatory bowel diseases. *Sci Adv*. 2022;8(45):eabp8798. doi:10.1126/sciadv.abp8798
14. Chen J, An X, Xu L, et al. Adhesive nanoparticle-in-microgel system with ROS scavenging capability and hemostatic activity for postoperative adhesion prevention. *Small*. 2024;20(27):e2306598. doi:10.1002/smll.202306598
15. Ye J, Fan Y, She Y, et al. Biomimetic self-propelled asymmetric nanomotors for cascade-targeted treatment of neurological inflammation. *Adv Sci*. 2024;11(22):e2310211. doi:10.1002/advs.202310211.
16. Wang Y, Zhang K, Li T, et al. Macrophage membrane functionalized biomimetic nanoparticles for targeted anti-atherosclerosis applications. *Theranostics*. 2021;11(1):164–180. doi:10.7150/thno.47841
17. Ni D, Wei H, Chen W, et al. Ceria nanoparticles meet hepatic ischemia-reperfusion injury: the perfect imperfection. *Adv Mater*. 2019;31(40):e1902956. doi:10.1002/adma.201902956.
18. Liu S, Xu J, Liu Y, et al. Neutrophil-biomimetic “nanobuffer” for remodeling the microenvironment in the infarct core and protecting neurons in the penumbra via neutralization of detrimental factors to treat ischemic stroke. *ACS Appl Mater Interfaces*. 2022;14(24):27743–27761. doi:10.1021/acsami.2c09020
19. Zhang W, Hu S, Yin -J-J, et al. Prussian blue nanoparticles as multienzyme mimetics and reactive oxygen species scavengers. *J Am Chem Soc*. 2016;138(18):5860–5865. doi:10.1021/jacs.5b12070
20. Yu H, Jin F, Liu D, et al. ROS-responsive nano-drug delivery system combining mitochondria-targeting ceria nanoparticles with atorvastatin for acute kidney injury. *Theranostics*. 2020;10(5):2342–2357. doi:10.7150/thno.40395
21. Zhang J, Cao Y, Wang C-A, et al. Design and preparation of MnO 2 /CeO 2 –Mn 2 double-shelled binary oxide hollow spheres and their application in CO oxidation. *ACS Appl Mater Interfaces*. 2016;8(13):8670–8677. doi:10.1021/acsami.6b00002.
22. Guo X, Li J, Jin X, et al. A hollow-structured manganese oxide cathode for stable Zn-MnO2 batteries. *Nanomaterials*. 2018;8(5):e1902956. doi:10.3390/nano8050301.
23. Zhou T, Ran J, Xu P, et al. A hyaluronic acid/platelet-rich plasma hydrogel containing MnO2 nanozymes efficiently alleviates osteoarthritis in vivo. *Carbohydr Polym*. 2022;292:119667. doi:10.1016/j.carbpol.2022.119667.
24. Sun Q, He F, Sun C, et al. Honeycomb-satellite structured pH/H $_2$ O $_2$ -responsive degradable nanoplatform for efficient photodynamic therapy and multimodal imaging. *ACS Appl Mater Interfaces*. 2018;10(40):33901–33912. doi:10.1021/acsami.8b10207
25. Sies H. Sies H hydrogen peroxide as a central redox signaling molecule in physiological oxidative stress: oxidative eustress. *Redox Biol*. 2017;11:613–619. doi:10.1016/j.redox.2016.12.035
26. Yang Y, Gu Z, Tang J, et al. MnO $_2$ nanoflowers induce immunogenic cell death under nutrient deprivation: enabling an orchestrated cancer starvation-immunotherapy. *Adv Sci*. 2021;8(4):2002667. doi:10.1002/advs.202002667
27. Zhang H, Cui Z, Luo G, et al. Ghrelin attenuates intestinal ischemia/reperfusion injury in mice by activating the mTOR signaling pathway. *IntJ Mol Med*. 2013;32(4):851–859. doi:10.3892/ijmm.2013.1452
28. Yang Z, Lin P, Chen B, et al. Autophagy alleviates hypoxia-induced blood-brain barrier injury via regulation of CLDN5 (claudin 5). *Autophagy*. 2020;17(10):3048–3067. doi:10.1080/15548627.2020.1851897.
29. Zhang X, Wei M, Fan J, et al. Ischemia-induced upregulation of autophagy preludes dysfunctional lysosomal storage and associated synaptic impairments in neurons. *Autophagy*. 2020;17(6):1519–1542. doi:10.1080/15548627.2020.1840796.
30. Popov SV, Mukhomedzyanov AV, Voronkov NS, et al. Regulation of autophagy of the heart in ischemia and reperfusion. *Apoptosis*. 2022;28 (1–2):55–80. doi:10.1007/s10495-022-01786-1
31. Randall-Demllo S, Chieppa M, Eri R. Eri R intestinal epithelium and autophagy: partners in gut homeostasis. *Front Immunol*. 2013;4:301. doi:10.3389/fimmu.2013.00301
32. Li D-L, Ding X-Y, Long J, et al. Identification of autophagy-related genes in diabetic foot ulcer based on bioinformatic analysis. *Int Wound J*. 2023;21(3):1–17. doi:10.1111/iwj.14476
33. Qin J, Zhang J, Wu -J-J, et al. Identification of autophagy-related genes in osteoarthritis articular cartilage and their roles in immune infiltration. *Front Immunol*. 2023;14:1–15. doi:10.3389/fimmu.2023.1263988
34. Yamamoto H, Zhang S, Mizushima N. Autophagy genes in biology and disease. *Nat Rev Genet*. 2023;24(6):382–400. doi:10.1038/s41576-022-00562-w.

35. Yang Y, Zhang M, Li Z, et al. Identification and cross-validation of autophagy-related genes in cardioembolic stroke. *Front Neurol*. 2023;14:1097623. doi:10.3389/fneur.2023.1097623.
36. Chen H, Pan Y, Zhou Q, et al. METTL3 inhibits antitumor immunity by targeting m6A-BHLHE41-CXCL1/CXCR2 axis to promote colorectal cancer. *Gastroenterology*. 2022;163(4):891–907. doi:10.1053/j.gastro.2022.06.024
37. Boada C, Zinger A, Tsao C, et al. Rapamycin-loaded biomimetic nanoparticles reverse vascular inflammation. *Circulation Res*. 2020;126(1):25–37. doi:10.1161/circresaha.119.315185.
38. Pape E, Parent M, Pinzano A, et al. Rapamycin-loaded poly(lactic-co-glycolic) acid nanoparticles: preparation, characterization, and in vitro toxicity study for potential intra-articular injection. *Int J Pharm*. 2021;609:121198. doi:10.1016/j.ijpharm.2021.121198
39. Li H, Wang X, Guo X, et al. Development of rapamycin-encapsulated exosome-mimetic nanoparticles-in-PLGA microspheres for treatment of hemangiomas. *Biomed Pharmacother*. 2022;148:112737. doi:10.1016/j.biopha.2022.112737
40. Guo X, Xu J, Huang C, et al. Rapamycin extenuates experimental colitis by modulating the gut microbiota. *J Gastroenterol Hepatol*. 2023;38 (12):2130–2141. doi:10.1111/jgh.16381
41. L KT, S GA, Haddad G, et al. Evaluation of off-label rapamycin use to promote healthspan in 333 adults. *GeroScience*. 2023;45(5):2757–2768. doi:10.1007/s11357-023-00818-1
42. L KJ, N RV, L WA, et al. Delayed-release rapamycin halts progression of left ventricular hypertrophy in subclinical feline hypertrophic cardiomyopathy: results of the RAPACAT trial. *J Ame Veterinar Med Assoc*. 2023:1–10. doi:10.2460/javma.23.04.0187.
43. Zhang F, Cheng T, Zhang S-X. Mechanistic target of rapamycin (mTOR): a potential new therapeutic target for rheumatoid arthritis. *Arthritis Res Therapy*. 2023;25(1):187. doi:10.1186/s13075-023-03181-w
44. Zheng L, Han X, Hu Y, et al. Dioscin ameliorates intestinal ischemia/reperfusion injury via adjusting miR-351-5p/MAPK13-mediated inflammation and apoptosis. *Pharmacol Res*. 2019;139:431–439. doi:10.1016/j.phrs.2018.11.040.
45. Erling N, De Souza Montero EF, Sannomiya P, et al. Local and remote ischemic preconditioning protect against intestinal ischemic/reperfusion injury after supraceliac aortic clamping. *Clinics*. 2013;68(12):1548–1554. doi:10.6061/clinics/2013(12)12.
46. Wang W, Li B, Wu Y, et al. Macrophage-derived biomimetic nanoparticles for light-driven theranostics toward Mpox. *Matter*. 2024;7 (3):1187–1206. doi:10.1016/j.matt.2024.01.004
47. Li C, Zhao Z, Luo Y, et al. Macrophage-disguised manganese dioxide nanoparticles for neuroprotection by reducing oxidative stress and modulating inflammatory microenvironment in acute ischemic stroke. *Adv Sci*. 2021;8(20):2101526. doi:10.1002/advs.202101526.
48. Tolstoy VP, Vladimirova NI, Gulina LB. Formation of ordered honeycomb-like structures of manganese oxide 2D nanocrystals with the birnessite-like structure and their electrocatalytic properties during oxygen evolution reaction upon water splitting in an alkaline medium. *ACS Omega*. 2019;4(26):22203–22208. doi:10.1021/acsomega.9b03499
49. Mosmann T. Mosmann T rapid colorimetric assay for cellular growth and survival: application to proliferation and cytotoxicity assays. *J Immunol Methods*. 1983;65(1–2):55–63. doi:10.1016/0022-1759(83)90303-4.
50. Li Y, Wen S, Yao X, et al. MicroRNA-378 protects against intestinal ischemia/reperfusion injury via a mechanism involving the inhibition of intestinal mucosal cell apoptosis. *Cell Death Dis*. 2017;8(10):e3127–e3127. doi:10.1038/cddis.2017.508
51. Chiu CJ, McArdle AH, Brown R, et al. Intestinal mucosal lesion in low-flow states. I. A morphological, hemodynamic, and metabolic reappraisal. *Arch Surg*. 1970;101(4):478–483. doi:10.1001/archsurg.1970.01340280030009
52. Chen H, He J. Facile synthesis of monodisperse manganese oxide nanostructures and their application in water treatment. *J Phys Chem C*. 2008;112 (45):17540–17545. doi:10.1021/jp806160g
53. Dai Y, Mao Z, Han X, et al. MicroRNA-29b-3p reduces intestinal ischaemia/reperfusion injury via targeting of TNF receptor-associated factor 3. *Br J Pharmacol*. 2019;176(17):3264–3278. doi:10.1111/bph.14759
54. Shen Y, Xin Z, Hu X, et al. Dual stimulus-responsive core-satellite SERS nanoprobes for reactive oxygen species sensing during autophagy. *Talanta*. 2022;250:123712. doi:10.1016/j.talanta.2022.123712
55. Zhou M, Zhang T, Zhang B. A DNA nanostructure-based neuroprotectant against neuronal apoptosis via inhibiting toll-like receptor 2 signaling pathway in acute ischemic stroke. *ACS Nano*. 2022;16(1):1456–1470. doi:10.1021/acsnano.1c09626
56. Lin T, Zhang Q, Yuan A, et al. Synergy of tumor microenvironment remodeling and autophagy inhibition to sensitize radiation for bladder cancer treatment. *Theranostics*. 2020;10(17):7683–7696. doi:10.7150/thno.45358.
57. Li L, Xiao B, Mu J, et al. A MnO_2 nanoparticle-dotted hydrogel promotes spinal cord repair *via* regulating reactive oxygen species microenvironment and synergizing with mesenchymal stem cells. *ACS Nano*. 2019;13(12):14283–14293. doi:10.1021/acsnano.9b07598.
58. Wang W, Wang J, Hu Z, et al. Advancing aggregation-induced emission-derived biomaterials in viral, tuberculosis, and fungal infectious diseases. *Aggregate*. 2024:e715. doi:10.1002/agt2.715.